

Published in final edited form as:

Nat Neurosci. 2017 July ; 20(7): 960–968. doi:10.1038/nn.4566.

Causal evidence for retina dependent and independent visual motion computations in mouse cortex

Daniel Hillier¹, Michele Fiscella², Antonia Drinnenberg¹, Stuart Trenholm¹, Santiago B. Rompani¹, Zoltan Raics¹, Gergely Katona³, Josephine Juettner¹, Andreas Hierlemann², Balazs Rozsa^{3,4}, and Botond Roska^{1,5,#}

¹Neural Circuits Laboratory, Friedrich Miescher Institute, 4058 Basel, Switzerland ²ETH Zurich, Bio Engineering Laboratory, 4058 Basel, Switzerland ³Two-photon Imaging Center, Institute of Experimental Medicine, Hungarian Academy of Sciences, Budapest, Hungary ⁴The Faculty of Information Technology, Pázmány Péter Catholic University, Budapest, Hungary ⁵Department of Ophthalmology, University of Basel, Basel, Switzerland

Abstract

How neuronal computations in the sensory periphery contribute to computations in the cortex is not well understood. We examined this question in the context of visual-motion processing in the retina and primary visual cortex (V1) of mice. We disrupted retinal direction selectivity – either exclusively along the horizontal axis using *FRMD7* mutants or along all directions by ablating starburst amacrine cells – and monitored neuronal activity in layer 2/3 of V1 during stimulation with visual motion. In control mice, we found an overrepresentation of cortical cells preferring posterior visual motion, the dominant motion direction an animal experiences when it moves forward. In mice with disrupted retinal direction selectivity, the overrepresentation of posterior-motion-preferring cortical cells disappeared, and their response at higher stimulus speeds was reduced. This work reveals the existence of two functionally distinct, sensory-periphery-dependent and -independent computations of visual motion in the cortex.

Users may view, print, copy, and download text and data-mine the content in such documents, for the purposes of academic research, subject always to the full Conditions of use:http://www.nature.com/authors/editorial_policies/license.html#terms

Corresponding author: Botond Roska (botond.roska@fmi.ch).

Code availability.

Analysis software can be downloaded from http://www.fmi.ch/groups/roska.b/NN2017_analysis.zip

Data availability.

The data that support the findings of this study are available from the corresponding author upon reasonable request.

Author Contribution. D.H. designed, performed, and analyzed cortical and LGN experiments, analyzed retinal experiments, performed optokinetic reflex experiments, guided the design and development of software, wrote the real-time response detection algorithm, performed retinal immunohistochemistry, and wrote the paper. M.F. designed, performed, and analyzed retinal experiments. A.D. performed and analyzed retinal experiments on *Drd4-GFP* and *Hb9-GFP* mice. S.T. performed cortical experiments, pupillary and optokinetic reflex recordings, and analyzed optokinetic reflex data. Z.R. developed software. K.G. and Ba.R. developed the 3D two-photon microscope and K.G., D.H. and Ba.R. developed corresponding software. S.R. performed cortex immunohistochemistry. J.J. developed and made the AAVs. A.H. guided the design and development of the microelectrode arrays. Bo.R. designed experiments, analyzed data, and wrote the paper.

Competing Financial Interest. The authors declare no competing financial interest.

Introduction

Mammals process sensory stimuli in both the sensory periphery and the cortex. How computations in the sensory periphery contribute to computations in the cortex is not well understood. In the visual system, the primary visual cortex (V1) contains cells that respond preferentially to motion in a particular direction¹. The neuronal circuits that are responsible for computing these direction-selective responses were thought to be within the cortex^{2,3} or in the thalamus⁴. However, direction-selective responses have been found in the retina of a number of species^{5,6}, including mice. The majority of ON-OFF direction-selective retinal ganglion cells (ON-OFF DS cells) project to the lateral geniculate nucleus (LGN)^{7–9}, a part of the thalamus that receives input from the retina and relays it to V1. ON-OFF DS cells form 15% of retinal ganglion cells in mice⁸. Four types of retinal ON-OFF DS cells have been described, each providing the largest responses to motion in one of the four cardinal directions^{7–11}. Direction-selective responses have been measured in LGN cell bodies^{12,13} and axon terminals^{14,15}, suggesting that ON-OFF DS cells could contribute to the computation of direction selectivity in the cortex. However, no causal link between retinal and cortical computations of direction selectivity has been established, leaving the questions unanswered whether and what form of cortical direction selectivity is linked to retinal direction selectivity.

To gain insight into these questions, we disrupted retinal direction selectivity *in vivo* using two independent genetic approaches, and recorded neuronal responses to visual motion in V1 (Fig. 1a). In the first approach, we used *FRMD7* mutant mice (*FRMD7tm* mice), in which horizontal direction selectivity in the retina is missing but vertical direction-selective responses persist¹⁶, as a model system to study the contribution of retinal horizontal direction selectivity to cortical horizontal direction selectivity. In wild-type mice, *FRMD7* is specifically expressed in starburst amacrine cells, the interneuron type that provides asymmetric inhibition to direction-selective retinal ganglion cells. This asymmetric inhibition is necessary for direction selectivity. In *FRMD7tm* mice, the loss of horizontal direction selectivity is caused by the transition from asymmetric to symmetric inhibitory input from starburst amacrine cells. *FRMD7* is not expressed in the LGN or V1¹⁶. In the second approach, we ablated starburst cells genetically. It has been shown before that ablating starburst amacrine cells in the retina leads to the loss of retinal direction selectivity¹⁷.

In both *FRMD7tm* and starburst-cell-ablated mice we found that a form of cortical direction selectivity is abolished when retinal direction selectivity is disrupted. This retina-dependent form of direction selectivity is tuned to higher stimulus speeds and is present along the horizontal cardinal axis in the posterior direction. The remaining cortical direction selectivity is distributed more evenly across different stimulus speeds and directions. Therefore, our results suggest the existence of two functionally distinct computations of visual motion in the cortex, one that originates in the retina and one that is computed in circuits downstream of the retina.

Results

In *FRMD7tm* mice posterior-motion-preferring ON-OFF DS cells respond uniformly to motion in all directions

The lack of horizontal direction selectivity in the retina of *FRMD7tm* mice could result from horizontal direction selective cells either spiking to all stimulus directions or not responding to motion in any direction¹⁶. We determined which of these mechanisms acts in a type of ON-OFF DS cell that prefers a horizontal direction in wild type mice and projects to the LGN. We crossed *Drd4-GFP* mice, in which posterior-motion-preferring (motion direction refers to direction in the visual field) ON-OFF DS cells are labeled⁷, with *FRMD7tm* mice. Using two-photon targeted patch clamp recordings in isolated retinas we recorded spiking activity from GFP-labeled cells in *Drd4-GFP* retinas (control) and from GFP-labeled cells in *Drd4-GFP* × *FRMD7tm* retinas (Fig. 1b-g, Supplementary Fig. 1, *Drd4-GFP*, n = 12 cells from 3 mice, *Drd4-GFP* × *FRMD7tm*, n = 16 cells from 3 mice).

GFP-labeled cells in control retinas showed direction-selective responses to visual stimuli moving in eight different directions at a speed of 40 visual degrees/s ($^{\circ}$ /s, Fig. 1c, Supplementary Fig. 1a). In contrast, GFP-labeled cells in *Drd4-GFP* × *FRMD7tm* retinas were not direction selective (Fig. 1d-f, Supplementary Fig. 1b, Kolmogorov-Smirnov test, $p = 4.5 \times 10^{-6}$) and showed uniform responses to all directions of motion (Fig. 1d, e, Supplementary Fig. 1b, Hodges-Ajne test, $p = 0.44$). The uniform responses were mostly due to an increase in firing in non-preferred directions (Fig. 1d, e, Supplementary Fig. 1b). The distribution of firing rates across all stimulus directions was shifted to higher frequencies in *FRMD7tm* mice (Fig 1g, Mann-Whitney U test, $p = 3.3 \times 10^{-9}$). Therefore, posterior-motion-preferring ON-OFF DS cells projecting to the LGN lose direction selectivity in *FRMD7tm* retinas by responding uniformly to motion in all directions.

In starburst-cell-ablated mice, ON-OFF DS cells respond uniformly to motion in all directions

We then abolished retinal direction selectivity acutely in adult mice. To selectively ablate starburst cells in adult mice, we crossed mice expressing Cre recombinase in starburst cells (*ChAT-Cre18*) with mice conditionally expressing the diphtheria toxin receptor (*LSL-DTR19*). Injecting diphtheria toxin (DT) into the eyes of *ChAT-Cre* × *LSL-DTR* mice led to the complete loss of starburst cells ('starburst-ablated mice'), seven days after injection, shown by immunohistochemistry using a ChAT antibody which selectively labels starburst cells (Supplementary Fig. 2, Supplementary Fig. 3). The number of retinal cells in other defined cell populations (that did not include starburst cells) did not change significantly (Supplementary Fig. 3). In all our experiments involving starburst ablation (in the retina, LGN, or cortex), we injected DT into both eyes and post-hoc stained both retinas with the ChAT antibody. We only considered those experiments for analysis in which we confirmed complete loss of starburst cells in both eyes.

We determined the effect of starburst ablation on the activity of a single, genetically defined type of ON-OFF DS cell by crossing *Hb9-GFP* mice, in which dorsal-motion-preferring ON-OFF DS cells are labeled²⁰, with *ChAT-Cre* and *LSL-DTR* mice. Using two-photon

targeted patch clamp recordings in isolated retinas, we recorded spiking activity from GFP-labeled cells in DT-injected *Hb9-GFP* retinas (control) and from GFP-labeled cells in *Hb9-GFP* starburst-ablated retinas (Fig. 2a-f, *Hb9-GFP*, n = 18 cells from 5 mice, *Hb9-GFP* starburst-ablated, n = 19 cells from 5 mice). GFP-labeled cells in control retinas showed direction-selective responses to visual stimuli moving at 40 °/s (Fig. 2b, Supplementary Fig. 4a). In contrast, GFP-labeled cells in starburst-ablated retinas were not direction selective at this speed, where direction-selective responses in *Hb9-GFP* mice are known to depend on starburst inhibition²⁰ (Fig. 2c-e, Supplementary Fig. 4b, Kolmogorov-Smirnov test, $p = 2.2 \times 10^{-8}$). GFP-labeled cells in starburst-ablated retinas showed uniform responses to all directions of motion (Fig. 2c, d, Supplementary Fig. 4b, Hodges-Ajne test, $p = 0.94$). The uniform responses were mostly due to an increase in firing in non-preferred directions (Fig. 2c, d, Supplementary Fig. 4b). The distribution of firing rates across all stimulus directions was shifted to higher frequencies in starburst-ablated mice (Fig. 2f, Mann-Whitney U test, $p = 1.8 \times 10^{-11}$).

We then tested the effect of starburst cell ablation on the visual-motion-evoked spiking activity of retinal ganglion cells at the population level in isolated retinas using high-density microelectrode arrays²¹ (Fig. 3, control, n = 1008 cells from 5 mice, starburst-ablated, n = 1199 cells from 5 mice). Wild type mice in which DT was injected into both eyes served as control here and in all subsequent experiments in retina and cortex involving starburst-ablation. Starburst cell ablation resulted in a 93% decrease in direction-selective spiking responses in the retina of *ChAT-Cre* × *LSL-DTR* mice (Fig. 3e, Fisher's exact test, $p = 1.1 \times 10^{-12}$, control, 5.37%, starburst-ablated, 0.40% direction-selective responses at direction selectivity index (DSI) > 0.5). ON-OFF ganglion cells in starburst-ablated retinas responded to motion, but the responses were uniform in all directions (Fig. 3c, d, Hodges-Ajne test, $p = 0.16$). The distribution of firing rates of the entire recorded ganglion cell population in response to motion across all eight directions in starburst-ablated retinas was shifted slightly, but significantly, to higher frequencies than in control retinas (Fig. 3f, Mann-Whitney U test, $p = 8.0 \times 10^{-53}$). The firing rates in uninjected (n = 1074 cells from 5 mice) and DT-injected wild type mice were similar (Fig. 3g, Mann-Whitney U test, $p = 0.075$). Starburst-ablation did not affect the proportion of ON-OFF cells (Fisher's exact test, $p = 0.67$, control, 33.0%, starburst-ablated, 33.7% of ON-OFF responses at ON-OFF index (OOI) < 0.3) or the proportion of orientation-selective cells (Fisher's exact test, $p = 0.89$, control, 4.4%, starburst-ablated, 4.3% orientation-selective responses at orientation selectivity index (OSI) > 0.2 and DSI < 0.2).

The starburst ablation experiments described so far were performed *ex vivo* in isolated retinas. To assess how the activity of retinal ganglion cells is affected by starburst ablation *in vivo*, we injected an AAV expressing GCaMP6s into the eyes of control and starburst-ablated mice (*ChAT-Cre* × *LSL-DTR* + DT). We then imaged (Fig. 4a, b, Methods) the axon terminals of GCaMP6s-expressing ganglion cells in the outer shell region of the LGN (control, n = 73 responding terminals from 2 mice, starburst-ablated, n = 132 responding terminals from 3 mice). In control mice, axon terminals fell into three groups with qualitatively different responses. The first group had direction-selective responses with direction tuning along the cardinal directions. The second group had orientation-selective responses, mostly vertically oriented. The third group had no direction or orientation

preference. In starburst-ablated mice we found no direction-selective axon terminals (Fig. 4c), and the distribution of DSIs shifted significantly to lower values (Fig. 4d, Fisher's exact test, $p = 8.1 \times 10^{-8}$, control, 17.8%, starburst-ablated, 0.0% direction-selective axon terminals, at $DSI > 0.5$), indicating a decrease in direction selectivity. Similar to the *ex vivo* retinal recordings, the peak responses of ganglion cell axon terminals in starburst-ablated mice were slightly, but significantly, higher than those in control mice (Fig. 4e, Mann-Whitney U test, $p = 1.0 \times 10^{-6}$). Consistent with the lack of change in the proportion of retinal orientation-selective responses *ex vivo*, the proportion of orientation-selective responses *in vivo* was also similar (Fisher's exact test, $p = 0.31$, control, 39.7%, starburst-ablated, 47.7% orientation-selective responses in axon terminals, at $OSI > 0.2$ and $DSI < 0.2$). The response amplitudes of vertical orientation-selective axon terminals were similar in control and starburst-ablated mice (Fig. 4f, Mann-Whitney U test, $p = 0.1$), suggesting that the activity of this ganglion cell type^{22,23} is unaffected by starburst ablation. We found an increase in the proportion of non-selective terminals (Fisher's exact test, $p = 0.0016$, control, 4.1%, starburst-ablated, 19.7%, at $OSI < 0.2$ and $DSI < 0.2$), which is consistent with ON-OFF DS cells being direction non-selective in starburst-ablated mice. The large increase in the proportion of non-selective terminals is likely due to the high density of ON-OFF DS cell axon terminals in the outer shell region¹⁴ of the LGN where we performed imaging. These results show that starburst cell ablation affected the activity of direction-selective retinal ganglion cells similarly *in vivo* and *ex vivo*.

Visual behavior in starburst-cell-ablated mice

We used two behavioral tests to determine the effect of starburst ablation on the activity of retinal ganglion cells. First we tested the pupil reflex, which depends predominantly on the activity of melanopsin-containing, direction non-selective ganglion cells²⁴. We found no difference in the pupil reflex between control and starburst-ablated mice (Supplementary Fig. 5a, b, Mann-Whitney U test, $p = 0.886$, control, $n = 4$ mice, starburst-ablated, $n = 4$ mice), indicating that starburst cell ablation left the melanopsin-containing ganglion cells and their retinal circuits intact. Second, we tested the optokinetic reflex, which relies on direction-selective ganglion cells and has previously been shown to become dysfunctional upon the loss of starburst cells¹⁷. The optokinetic reflex was lost after DT injection in *ChAT-Cre* \times *LSL-DTR* mice but remained intact when DT was injected into wild type mice (Supplementary Fig. 5c, d, Mann-Whitney U test, $p = 0.002$, control, $n = 6$ mice, starburst-ablated, $n = 6$ mice).

Diphtheria toxin acts locally in the eye

In *ChAT-Cre* mice, a population of cortical cells also expresses Cre recombinase (Supplementary Fig. 6). To determine if the injection of DT into the eye affects cortical circuits by DT leaking out from the eye and locally ablating Cre- and DTR-expressing cortical cells, we crossed *ChAT-Cre*, *LSL-DTR* and *LSL-tdTomato* mice and compared the density of tdTomato-expressing cells in V1 in DT-injected and uninjected (control) *ChAT-Cre* \times *LSL-DTR* \times *LSL-tdTomato* mice. We found no significant difference between the densities of tdTomato-expressing cells in V1 (Supplementary Fig. 6, Mann-Whitney U test, $p = 0.40$, control, $125 \text{ cells/mm}^3 \pm 4 \text{ s.e.m}$, $n = 3$ mice, starburst-ablated, $132 \text{ cells/mm}^3 \pm 10 \text{ s.e.m}$, $n = 3$ mice), despite the loss of starburst cells in the retina of DT-injected mice.

Furthermore, *ChAT-Cre* × *LSL-DTR* mice showed no apparent differences in motor behavior before and after DT injection, suggesting that the cholinergic motor neurons, which also express the DT receptor, were not affected by the DT injection into the eye. Together, these results indicate that DT does not spread out after being injected into the eye, but acts locally within the eye.

One form of cortical direction selectivity relies on retinal direction selectivity

We then investigated how the disruption of retinal direction selectivity affects cortical direction selectivity in either *FRMD7tm* (Fig. 5, control of *FRMD7tm*, n = 4961 cells from 9 mice, *FRMD7tm*, n = 4379 cells from 9 mice) or starburst-ablated mice (Fig. 6, control of starburst-ablated, n = 1669 cells from 4 mice, starburst-ablated, n = 1632 cells from 4 mice). We compared the distribution of direction-selective cells in layer 2/3 of V1 (cortical DS cells) in control mice and in mice with disrupted retinal direction selectivity by imaging neuronal activity using genetically-encoded calcium sensors: GCaMP6s in *FRMD7tm* and its control mice; and GCaMP6f25 in starburst-ablated and its control mice. We used AAV serotype 1 delivered by cortical injection or PHP.B serotype26 delivered by intravenous injection (the latter mentioned specifically for the corresponding experiments). The advantage of serotype PHP.B AAV is that it leads to widespread labeling of cortical cells and yields no nuclear expression of GCaMP6 for at least 10 weeks, the latest time we tested. We stimulated one eye with gratings moving in eight directions at 40 °/s, and recorded neuronal activity in the contralateral V1 (Fig. 5a, Fig. 6a).

In control mice, the distribution of cortical DS cells across different preferred directions (Fig. 5b, Fig. 6b) showed a significant bias to posterior motion²⁷ (Fig. 5d, e, Fig. 6d, e, Hodges-Ajne test, control of *FRMD7tm*, $p = 9.7 \times 10^{-47}$, control of starburst-ablated, $p = 5.5 \times 10^{-17}$, at DSI > 0.5): 27.0% (control of *FRMD7tm*) and 26.8% (control of starburst-ablated) of cortical DS cells preferred posterior motion (at DSI > 0.5). In contrast, cortical DS cells in mice with disrupted retinal direction selectivity (Fig. 5c, Fig. 6c) were not biased to posterior motion: a significantly smaller fraction, only 10.3% (*FRMD7tm*) and 6.2% (starburst-ablated), preferred posterior motion (Fig. 5d, e, Fig. 6d, e, Fisher's exact test, *FRMD7tm* $p = 1.9 \times 10^{-18}$, starburst-ablated $p = 3.7 \times 10^{-11}$, at DSI > 0.5). Together with the decrease in the proportion of posterior-motion-preferring cortical DS cells, we found a significant increase in the proportion of dorsal-motion-preferring cortical DS cells (Fig. 5d, Fig. 6d, Fisher's exact test, *FRMD7tm*, $p = 0.0003$, starburst-ablated, $p = 0.01$, at DSI > 0.5). Therefore, the balance between the representation of horizontal and vertical directions, quantified with a selectivity index (Methods), significantly changed between control mice and mice with disrupted retinal direction selectivity (Fig. 5f, Fig. 6f, Fisher's exact test, *FRMD7tm*, $p = 3.1 \times 10^{-12}$, starburst-ablated, $p = 1.2 \times 10^{-8}$, at DSI > 0.5) while the overall distribution of direction-selective cells remained similar (Mann-Whitney U test, Fig. 5g, $p = 0.81$, control of *FRMD7tm*, 46.25%, *FRMD7tm*, 41.66%; Fig. 6g, $p = 0.39$, control of starburst-ablated 26.6%, starburst-ablated, 28.4%, at DSI > 0.5). The proportion of direction-selective cells was different in the control of *FRMD7tm* and in the control of starburst-ablated mice, which was likely due to the use of different promoters or sensors (control of *FRMD7tm*, promoter: EF1a, sensor: GCaMP6s; control of starburst-ablated, promoter: hSyn, sensor: GCaMP6f).

Similar to the distribution of cortical DS cells according to their preferred directions (Fig. 5, Fig. 6), the distribution of response amplitudes of cortical DS cells also showed a significant bias to posterior motion and this bias was not present in mice with disrupted retinal direction selectivity (Supplementary Fig. 7). Despite the slight increase in overall activity in the retina (Fig. 3f), the average activity levels of responding cortical cells were similar between control mice and mice with disrupted retinal direction selectivity (Supplementary Table 1). This maintained activity level is consistent with previous reports that the amplitude distribution of cortical cells is under homeostatic control^{28,29}.

We examined the robustness of the finding that the proportion of posterior-motion-preferring cortical DS cells decreases in mice with disrupted retinal direction selectivity. First, we analyzed whether the decrease in the proportion of posterior-motion-preferring cortical DS cells depends on the choice of inclusion criteria for defining cells as ‘responding’. So far, we have defined a cortical cell as ‘responding’ if its response to the stimulus moving in any of the directions was above the response threshold for a contiguous block of at least one second for at least two repetitions of the stimulus. When we relaxed this definition to include cells that responded to at least one stimulus presentation, the reduced cortical representation of posterior motion remained significant (Supplementary Fig. 8). Second, we tested whether the decrease in the proportion of posterior-motion-preferring cortical DS cells depends on the number of stimulus repetitions. We infected mice intravenously with AAV PHP.B serotype expressing GCaMP6s. We stimulated one eye with gratings moving in eight directions at 40 °/s, and recorded neuronal activity in the contralateral V1 in control and *FRMD7tm* mice (control, n = 595 cells from 4 mice, *FRMD7tm* n = 403 cells from 4 mice). We presented the stimulus six times in each imaging plane and analyzed the distribution of cortical DS cells as a function of stimulus repetitions. The decrease in the proportion of posterior-motion-preferring cortical DS cells was significant at each number of stimulus repetitions, from two to six (Supplementary Fig. 9). Therefore, the observed difference between the distributions of cortical DS cells in control mice and in mice with disrupted retinal direction selectivity does not depend on the stringency of response inclusion criteria or on the number of stimulus repetitions.

In the retina, the spike frequency of ON-OFF DS cells monotonically increases with stimulus speed up to around 40 °/s^{11,30}. We therefore investigated whether the speed of the stimulus affected the responses of posterior-motion-preferring cortical DS cells in control and *FRMD7tm* mice differently. We infected mice intravenously with AAV PHP.B serotype expressing GCaMP6s (Fig. 7a). We stimulated mice with visual motion in eight different directions moving at 10, 16.6, 26.6, and 40 °/s and quantified the posterior component of the responses of cortical DS cells (Methods) as a function of stimulus speed. In control mice, the response monotonically increased with speed, while in *FRMD7tm* mice the response did not increase with speed (Fig. 7b, Kruskal-Wallis H test, p = 0.71, control, n = 1574 cells from 4 mice, *FRMD7tm*, n = 1342 cells from 4 mice, at DSI > 0.5).

Discussion

Our results show the existence of two different forms of direction selectivity in mouse visual cortex, each with distinct functional properties. One form of cortical direction selectivity,

which is tuned to higher stimulus speeds and is present along a cardinal direction, the posterior direction, relies on direction selectivity computed within the retina. A second form of cortical direction selectivity, which is distributed more evenly across different stimulus speeds and directions, is computed by circuits downstream from the retina, possibly within the cortex or in the LGN. Therefore, cortical computations expand feature-selectivity computed in the periphery to a larger dynamic range in at least two stimulus dimensions: speed and direction.

In visual cortex, our analysis detected the influence of retinal direction selectivity only on posterior-motion-preferring cells in layer 2/3, despite the fact that our retinal manipulations disrupted retinal direction selectivity either along two (*FRMD7tm* mice) or all four (starburst-ablated mice) cardinal directions. One explanation for this is a biased retinal direction representation combined with cortical plasticity following our manipulation of retinal direction selectivity. Posterior-motion-preferring ON-OFF DS cells labeled in *Drd4-GFP* mice outnumber dorsal-motion-preferring cells labeled in *Hb9-GFP* mice by 3.5 to 17,20, suggesting a dominance of posterior-motion-preferring cells in the retina⁹, which could lead to the overrepresentation of posterior-motion-preferring cortical DS cells. It is possible that the loss of the major direction-selective retinal input, tuned to the posterior direction, leads to a compensatory increase in direction selectivity computed locally in the cortex. Indeed, we detected such a significant increase in the dorsal direction. This compensatory increase in cortical direction selectivity could mask the loss of retinal direction-selective input from the three less-represented cardinal directions in the retina.

It is interesting to note that, in animal species with laterally positioned eyes (such as mice and rabbits), posterior image motion is the most prevalent motion direction when the animal moves forward, which is the dominant mode of whole-body locomotion. It is possible that in animals with laterally positioned eyes, the strong influence of retinal posterior direction selectivity on cortical direction selectivity is an adaptation of the retina to the statistics of image motion. In contrast, in animals with frontally positioned eyes, such as non-human primates and humans, forward locomotion is expected to elicit less asymmetry in the distribution of motion directions on the retina. Whether retinal ON-OFF DS cells exist in non-human primates and humans and, if they do exist, how they contribute to vision are intriguing and open questions in neuroscience.

Online Methods

Animals

ChAT-Cre (strain: B6;129S6-*ChAT^{tm1(cre)Low}/J*, stock number: 006410), *LSL-DTR* (strain: C57BL/6-*Gt(ROSA)26Sor^{tm1(HBEGF)Awai}/J*, stock number: 007900), *LSL-tdTomato* (strain: B6;129S6-*Gt(ROSA)26Sor^{tm9(CAG-tdTomato)Hze}/J*, stock number: 007905), *Hb9-GFP* (strain: Tg(Hlxb9-GFP)1Tmj, stock number: 005029), and *Bl6* ('wild type', strain: C57BL/6J, stock number: 000664) were purchased from Jackson laboratories. *Drd4-GFP* (strain: Tg(Drd4-EGFP)W18Gsat/Mmnc, stock number: 000231-UNC) was obtained from MMRRC. *FRMD7tm* mice refer to the homozygous female or hemizygous male *FRMD7^{tm1a(KOMP)Wtsi}* mice, which were obtained from the Knockout Mouse Project (KOMP) Repository. Wild type mice in which DT was injected into both eyes served as

control in experiments performed with DT. Animals were between two and eight months old. Both males and females were used. All animal experiments and procedures were performed in accordance with standard ethical guidelines (European Communities Guidelines on the Care and Use of Laboratory Animals, 86/609/EEC) and were approved by the Veterinary Department of the Canton of Basel-Stadt.

Two-photon targeted patch clamp recordings in retina

For targeted recordings of GFP-labeled single types of retinal ON-OFF DS cells, retinas were isolated under dim red light in oxygenated Ringer's medium. Retinas were mounted ganglion-cell-layer-up on a filter paper (Millipore) in which a 2 mm × 2 mm window was cut to enable visual stimulation of the retina. During recording, the retina was continuously superfused with oxygenated Ringer's medium and the temperature was kept at 35-36°C. The two-photon microscope system for targeted patch-clamp recordings from GFP-expressing cells, including the light pathways for visual stimulation of the retina, has been described before³¹. Fluorescent cells were targeted using a two-photon microscope equipped with a Mai Tai HP two-photon laser (Spectra Physics), set to 920 nm, integrated into the electrophysiological setup. The two-photon fluorescent image was overlaid on an IR image acquired using a CCD camera (SPOT Visitron Systems). The infrared light was produced with a digital light projector (PLUS) and a 750±25 nm filter. Spike recordings were performed in loose cell-attached mode with 5-7 MΩ glass electrodes (BF100-50-10, Sutter Instruments) filled with Ringer's solution with a Multiclamp 700B amplifier (Molecular Devices). Signals were digitized at 10 kHz (National Instruments A/D board) and acquired using software written in LabVIEW (National Instruments). The light patterns for retinal stimulation were generated using a DLP projector (PLUS; refresh rate of 75 Hz) and focused on the retina, after passing a neutral density filter (ND30). The stimuli were controlled via software written in Python. Direction selectivity was tested by moving a 300 μm diameter white light spot (1000 R*/s light intensity) on black background across the retina in eight different directions at 1200 μm/s. All stimuli were repeated six times, the first repetition was excluded from analysis. Data was analyzed in Matlab and Python. Spikes were detected via thresholding.

Diphtheria toxin injection

Diphtheria toxin (DT) stock solution was made from diphtheria toxin (Sigma, D0564) dissolved in PBS (Phosphate Buffered Saline) at 2 μg/μl concentration and was stored at -80°C. Before eye injection, the stock was diluted with PBS to a final concentration of 1.76 ng/μl. Mice were anesthetized with fentanyl-medetomidine-midazolam (fentanyl 0.05 mg/kg, medetomidine 0.5 mg/kg, midazolam 5.0 mg/kg). A hole was made close to the border between sclera and cornea using a 30G needle. 2 μl toxin solution was loaded into a pulled borosilicate glass pipette (1.5 mm outer diameter, tip diameter 100 μm). The pipette was guided through the hole and the solution was injected into the vitreous. Both eyes were injected. After the eye injection, anesthesia was antagonized with a mix of naloxone 1.2 mg/kg, atipamezol 2.5 mg/kg, and flumazenil 0.5 mg/kg. Each eye was re-injected two days after the initial injection. Starburst-ablated recordings were performed seven days after the initial injection.

Antibody staining and confocal imaging

Retina: Antibody staining and confocal imaging was performed in whole-mount retinas as described before³². In all staining procedures four labels were used. Hoechst-labeling of the cell nuclei and ChAT-antibody-labeling of the starburst cells were included in all stainings. At the end of all physiological and imaging experiments involving DT injection, the presence of starburst cells was detected with immunostaining and the results were only analyzed if starburst cells were not detectable in the retina. The primary antibodies used were goat anti-ChAT (Chemicon, AB144P-200UL, 1:200), rabbit anti-GABA (Sigma, A2052, 1:2000), rabbit anti-calbindin D-28k (Swant, CB38, 1:1000), and rat anti-glycine (Immunosolution, IG1002, 1:7500). The secondary antibodies used were Alexa 555 anti-goat (Invitrogen, A21432), Alexa 488 anti-goat (Invitrogen, A11055), Alexa 488 anti-rabbit (Invitrogen, A21206), Cy3 anti-rabbit (Jackson ImmunoResearch, 711-165-152) and Cy5 anti-rat (Jackson ImmunoResearch, 711-175-153) all at a concentration of 1:200. Nuclei were stained with Hoechst (1:1000). Lectin peanut agglutinin (PNA) coupled to Alexa 568 (Invitrogen, L32458, 1:500) was used to label cones. Stained retinas were imaged using a Zeiss LSM 720 confocal microscope.

Brain slice: To quantify the number of ChAT positive cells per unit volume of V1 in DT-injected and uninjected *ChAT-Cre* × *LSL-DTR* × *LSL-tdTomato* mice, brains were isolated and fixed for two hours in 4% paraformaldehyde (PFA) and were then cut to 150 μm thick slices using a vibratome. Slices were washed with PBS three times for ten minutes then mounted and imaged under a 10× air objective in a Zeiss LSM 720 confocal microscope. *tdTomato*-expressing cells were counted manually. To quantify the proportion of cortical cells labeled by GCaMP6s and the proportion of cells colabeled with parvalbumin (PV) after intravenous delivery of serotype PHP.B AAV, mice were perfused for seven minutes with cold PBS containing 10 units/ml heparin, then for seven minutes with cold 4% PFA. Brains were dissected after perfusion and incubated in 4% PFA for two hours then sectioned at 150 μm thickness. Slices were washed with PBS three times for ten minutes then incubated with blocking solution (3% NDS, 1% BSA, 0.1% tritonX, 0.01% sodium azide) for two hours, incubated with primary antibodies for 48 hours, washed three times for ten minutes with PBS, incubated with secondary antibodies for two hours, washed three times for ten minutes with PBS, and mounted on glass slides with ProLong Gold (Thermo Fisher Scientific). Slices were imaged under a 20× air objective in a Zeiss 720 LSM confocal microscope. Cells were counted manually on a maximum intensity projection of the top 20 μm of a slice. The primary antibodies used were: guinea pig anti-PV (Synaptic Systems, 195 004, 1:500), rabbit anti-GFP (Millipore, AB3080, 1:500). Secondary antibodies used were: goat anti-guinea pig Alexa 647 (Thermo Fisher Scientific, A-21450, 1:500), donkey anti-rabbit Alexa 568 (Life technologies, A10042, 1:750).

Microelectrode array recordings

A CMOS-based microelectrode array was used for extracellular recordings from mouse retinal ganglion cells as described before^{33,34}. The array features 26,400 platinum electrodes at a density of 3265 electrodes/mm², and extracellular signals can be recorded simultaneously from an arbitrarily selectable and reconfigurable subset of maximum 1024 electrodes²¹. Spike sorting and light stimulation has been described before^{33,35}. Two light

stimuli were used. First, a flashed square stimulus was used to determine if a cell was ON-OFF type (responding to both light increments and decrements). A positive-contrast square (0.2 mm × 0.2 mm) was turned on for one second and turned off for one second in five repetitions. The stimulus moved sequentially in discrete non-overlapping steps over an area of $\approx 1\text{mm}^2$ with a background irradiance of $0.2\ \mu\text{W}/\text{cm}^2$ and a square stimulus irradiance of $47\ \mu\text{W}/\text{cm}^2$ (Michelson contrast = 0.99). Second, a grating with white and black bars, 300 and 900 μm wide, was moved at 1200 $\mu\text{m}/\text{s}$ in eight directions (Michelson contrast = 0.99). This stimulus was the same as the stimulus used in cortical experiments. The preferred direction was defined as the direction of motion of the grating stimulus that elicited the highest spike rate. The null direction was the 180° rotated direction with respect to the preferred direction.

Retinal response quantification

The direction selectivity index (DSI) and orientation selectivity index (OSI) were defined as described before³⁶:

$$\text{DSI} = \left| \frac{\sum_{j=1}^8 R_j e^{i\theta_j}}{\sum_{j=1}^8 R_j} \right|$$

$$\text{OSI} = \left| \frac{\sum_{j=1}^8 R_j e^{2i\theta_j}}{\sum_{j=1}^8 R_j} \right|$$

where R_j denotes the peak firing rate in each of the eight directions of stimulus movement ordered in ascending directions 0-360° in 45° steps. The following thresholds were used to define selective and non-selective cells. Direction-selective cell: $\text{DSI} > 0.5$, orientation-selective cell: $\text{OSI} > 0.2$ and $\text{DSI} < 0.2$, non-selective cell: $\text{OSI} < 0.2$ and $\text{DSI} < 0.2$.

ON-OFF versus not-ON-OFF cells were classified based on the responses to the flashed-square stimulus using an ON-OFF index (OOI).

$$\text{OOI} = \frac{R_{\text{ON}} - R_{\text{OFF}}}{R_{\text{ON}} + R_{\text{OFF}}}$$

where R_{ON} and R_{OFF} refer to the peak firing rates to the onset and offset of the positive-contrast square, respectively. A cell was defined as ON-OFF if $|\text{OOI}| < 0.3$.

The “peak firing rates” of a ganglion cell, in response to motion stimulation, were determined as follows. Spiking responses to five repetitions of stimuli moving in eight different directions were recorded. Each spiking response was binned (bin width=10 ms) and convolved with a Gaussian kernel ($\sigma=100\text{ms}$), resulting in five response curves. The maxima of the five response curves were averaged. The resulting single value was defined as the

peak firing rate. Using this algorithm, the peak firing rate for each stimulus direction was computed. Therefore, the peak firing rates of a single ganglion cell, in response to motion stimulation, were described with eight numbers, one for each direction. These eight numbers were normalized to their maximum (therefore scale from 0 to 1), yielding “normalized peak firing rates” which were plotted on polar plots in Fig. 1c,d, 2b,c. “peak firing rates” for flashed-square stimulus were defined similarly.

The “mean of the peak firing rates” of a group of ganglion cells, in response to motion stimulation, was determined as follows. The peak firing rate (defined above) in each stimulus direction was determined for each retinal ganglion cell of the group. This resulted in eight numbers for each recorded cell. These eight numbers were averaged across the group, resulting again in eight numbers, the mean of the peak firing rates of the group. “Normalized mean of the peak firing rates” was defined for two groups of retinal ganglion cells, the control and mutant groups, by taking the mean of the peak firing rates of both groups (2 x 8 numbers) and normalizing these 16 numbers to their maximum (scale from 0 to 1). Normalized means of the peak firing rates were plotted on polar plots in Fig. 1e, 2d, 3d.

The “complementary cumulative distribution of DSI values” of a group of retinal ganglion cells was determined as follows. The peak firing rate (defined above) for each of the eight stimulus directions was determined for each retinal ganglion cell of the group. This resulted in eight numbers for each recorded cell. Based on the eight numbers, a DSI value was calculated for each cell, resulting in “n” DSI values for the group of ganglion cells, where n is the number of cells in the group. The complementary cumulative distribution of these DSI values shows the proportion of cells with DSI larger than the value indicated on the x-axis and is equivalent to 1 minus the cumulative distribution. Complementary cumulative distributions of DSI values are shown in Fig. 1f, 2e, 3e.

The “complementary cumulative distribution of peak firing rates across all stimulus directions” of a group of retinal ganglion cells was determined as follows. The peak firing rate (defined above) for each of the eight stimulus directions was determined for each retinal ganglion cell of the group. This resulted in eight numbers for each recorded cell. These eight numbers were collected for all ganglion cells in the group resulting in n x 8 numbers (n=number of ganglion cells in the group). The complementary cumulative distribution (defined above) of the n x 8 numbers was called the complementary cumulative distribution of peak firing rates across all stimulus directions of the group, and was plotted in Fig. 1g, 2f, 3f,g.

Adeno-associated viruses (AAV)

AAVs were made as described previously³⁷. Genome copy (GC) number titration was performed using real-time PCR (Applied Biosystems, TaqMan reagents). Two different AAVs were used. The first AAV, AAV-EF1a-GCaMP6s-WPRE, was obtained by cutting commercially synthesized GCaMP6s with BamHI/EcoRI overhang sites (Genewiz Inc.) with BamHI/EcoRI. This was then inserted into pAAV-EF1a-DIO-hChR2(H134R)-EYFP-WPRE (kindly provided by K. Deisseroth) using BamHI/EcoRI sites. The serotype of this AAV was 1, PHP.B26 or 7. Serotype 1 (6.6×10^{12} GC/ml) was used in experiments in the cortex of

FRMD7tm and corresponding control mice (Fig. 5, Supplementary Fig. 7, 8) except for analyzing the influence of the number of stimulus repetitions and for determining the speed tuning of cortical cells. Serotype PHP.B (1.7×10^{14} GC/ml) was used in experiments in the cortex of *FRMD7tm* and corresponding control mice for analyzing the influence of the number of stimulus repetitions (Supplementary Fig. 9) and for determining the speed tuning of cortical cells (Fig. 7). Serotype 7 (3.5×10^{12} GC/ml) was used in experiments in the LGN of starburst-ablated and corresponding control mice (Fig. 4). The second AAV, AAV-hSyn-GCaMP6f-WPRE was generated by PCR amplifying the hSyn promoter from pAAV.hSyn.GCaMP3.3 (kindly provided by J.M. Wilson) flanked with MluI and BamHI restriction sites, and replacing the EF1a promoter in pAAV-EF1a-GCaMP6f-WPRE using MluI/BamHI digest. The serotype of this AAV was 1 (1.4×10^{12} GC/ml). This AAV was used in experiments in the cortex of starburst-ablated and corresponding control mice (Fig. 6, Supplementary Fig. 7, 8).

Viral injection to the eye

The procedure followed the diptheriatoxin injection protocol described above. 2 μ l serotype 7 AAV-EF1a-GCaMP6s-WPRE was loaded into a pulled borosilicate glass pipette and was injected into the vitreous. Only the eye contralateral to the imaged LGN was injected. LGN recordings were performed three weeks after the virus injection.

Two-photon imaging of ganglion cell axon terminals in the LGN

Mice were anesthetized as described for toxin injection and placed in a stereotaxic frame (Narishige, SR-5M). Colliquifilm (Allergan) was applied to the eyes to prevent dehydration during surgery. A metal bar for head fixation during imaging was glued to the skull³⁸. An 8 mm diameter craniotomy was made above the LGN. The exposed cortex and the underlying hippocampus were aspirated, exposing the LGN. The tissue was kept moist with a buffer (135 mM NaCl, 5.4 mM KCl, 5 mM HEPES, 1.8 mM CaCl₂, pH 7.2). A 2 mm diameter glass coverslip was slightly pushed against the LGN, while the tissue between the edges of the coverslip and the skull was covered with superglue and dental cement. After surgery, anesthesia was antagonized as described above for eye injections, and mice were left to recover on a heating pad for one hour. Before imaging, mice were anesthetized with 0.25% isoflurane and 2.5 mg/kg chlorprothixene. Retinal ganglion cell axons terminals in the LGN were imaged through a 16 \times objective (Nikon, 0.8 numerical aperture (NA)) down to 200 μ m depth. The rest of the imaging and stimulation procedure was the same as described below for cortical two-photon imaging and visual stimulation.

Optokinetic reflex and pupil reflex measurement

Eye tracking was performed using an ETL-200 eye tracking system (Iscan Inc., Woburn, Maine, USA). To visualize the pupil, eyes were illuminated with IR light and recorded with IR cameras at 120 Hz. The optokinetic response was quantified by counting the number of eye tracking movements (ETMs) as described previously³⁹. Briefly, the position of the pupil was plotted as a function of time, the derivative of this signal was calculated, and a threshold was set. Events above threshold were counted as ETMs. The threshold was adjusted in control mice so that all visually assessed ETMs were detected. This threshold was then applied to starburst-ablated mice. Visual stimulation was performed as described

previously⁴⁰, except that here two monitors were placed in a ‘V’ position in front of the mouse for binocular stimulation. The head of the mouse was fixed with a head holder, and the body was restrained in a foam jacket. For motion stimulation, black and white gratings (0.5 duty cycle) with 10°-wide bars were moved at 10°/s. 1° corresponds to 31 μm retinal distance in mice⁴¹. To test the pupil reflex of the mouse, the pupil diameter was measured first under dark conditions and then while a full-field white flash was shown to the mouse. White flash intensity was 40 μW/cm² measured at the screen surface.

Cranial-window implantation and virus injection to cortex

Mice were anesthetized as described above for toxin injections and placed in a stereotaxic frame (Narishige, SR-5M). Colliquifilm (Allergan) was applied to the eyes to prevent dehydration during surgery. A thin iron ring and a metal bar for head fixation during imaging were glued to the skull³⁸. A 3 mm diameter craniotomy was made above the primary visual cortex, 2.5 mm lateral from the medial blood vessel and 1.0 mm frontal from the coronal blood vessel. The cortical surface was kept moist with a buffer (135 mM NaCl, 5.4 mM KCl, 5 mM HEPES, 1.8 mM CaCl₂, pH 7.2). 100 nl AAV was slowly injected into the visual cortex at a depth of 100–400 μm using a borosilicate glass micropipette (tip diameter 30 μm) at multiple (3–5) sites. After viral injection, the cortex was covered with a 3 mm diameter glass coverslip and sealed with dental acrylic cement (Paladur, Heraeus Kulzer). Dental acrylic cement was also used to mount a head bar on the skull to immobilize the mouse during imaging³⁸.

Viral labeling of cortex by intravenous injection

Intravenous injection (Supplementary Fig. 10) was used for analyzing the influence of the number of stimulus repetitions and for determining the speed tuning of cortical cells. The advantage of intravenously delivered serotype PHP.B26 AAV was that it led to widespread labeling of cortical cells and yielded no nuclear expression of GCaMP6 for at least 10 weeks, the longest time tested (Supplementary Fig. 11). Mice were anesthetized with 5% isoflurane and received a single retro-orbital injection⁴² of 10 μl serotype PHP.B AAV-EF1a-GCaMP6s-WPRE. Cortical recordings were performed from three weeks after injection. The proportion of visually responsive cells in layer 2/3 of the V1 infected by intravenous injection of serotype PHP.B AAV was slightly lower than the proportion of visually responsive cells infected by direct cortical injection of serotype 1 AAV (Mann-Whitney U test, $p = 0.03$, intravenous injection, $9.21\% \pm 1.65\%$ s.e.m, $n = 16$ mice, direct injection, $12.1\% \pm 1.58\%$ s.e.m, $n = 18$ mice). The proportion of visually responsive cells was quantified as follows. We stimulated and extracted responding cells as described below in “Cortical two-photon imaging and visual stimulation” and “Online response detection”. We included calcium traces recorded during both the static and the moving part of the stimulus. Visually responsive cells were defined as described before⁴³, using ANOVA ($p < 0.01$) and a threshold $F/F > 0.05$ in the direction with largest amplitude. After intravenously delivery of AAV-Ef1a-GCaMP6s-WPRE, 22.2% of the cells in V1 were labeled with GCaMP6. The proportion of PV-and-GCaMP6 colabeled cells among GCaMP6-labeled cells was 8.4%, similar to the proportion of PV-labeled cells among all V1 cells (7.4%) (Supplementary Fig. 11).

Cortical two-photon imaging and visual stimulation

The activity of neurons in V1 was recorded by imaging fluorescence using a two-photon microscope (Femtonics, Femto3D-RC) and a mode-locked Ti:Sapphire laser (Newport, Mai Tai DeepSee) at 920 nm through either a 20× (Olympus, 0.95 NA) or a 16× (Nikon, 0.8 NA) water-immersion objective. During imaging, mice were anesthetized with 0.25% isoflurane and 2.5 mg/kg chlorprothixene and vital signs such as heart rate, breathing rate, and oxygen saturation were monitored (Starr Life Sciences, Mouse Ox). To shield light coming from the stimulation screen, a metal cone with a magnetic base ring was mounted on the head by attaching it to the iron ring. 1% low melting point agar solution with a black pigment (Lukas) was used to fill in the gaps between the cone and the metal ring on the head of the mouse.

A Python-based user interface controlled visual stimulation, data recording, and alignment. Scanning was performed in a horizontal plane at 6-8 Hz between 100 and 250 μm below the surface of the cortex in 10 μm steps (Supplementary Fig. 12). Visual stimulation was performed with an LED projector (Acer, K10), projecting images onto a 40 cm \times 29 cm (width \times height) screen positioned 28 cm from the right eye. We presented moving gratings in eight directions. The widths of the white and black bars of the grating were 10 and 30 visual degrees respectively (10 visual degrees translate to about 300 μm on the retina). The speed of the grating was 40 visual degrees/s ($^{\circ}/\text{s}$, 1200 $\mu\text{m}/\text{s}$ on the retina) for most cortical experiments, except for the experiments performed to estimate the speed tuning. Here mice were stimulated with the same grating moving at four distinct speeds: 10, 16.6, 26.6 and 40 $^{\circ}/\text{s}$ (300 $\mu\text{m}/\text{s}$, 500 $\mu\text{m}/\text{s}$, 800 $\mu\text{m}/\text{s}$, and 1200 $\mu\text{m}/\text{s}$ on the retina). The average stimulus intensity at the animal's eye was 2.2 $\mu\text{W}/\text{cm}^2$, Michelson contrast was 0.99. The grating, with an orientation orthogonal to the future motion direction, was first presented on the screen for 3.8 s. It then moved in one of eight directions (0, 45, 90, 135, 180, 225, 270, 315 degrees) for 3.8 s, and finally remained motionless on the screen for 4 s. With the exception of the experiments testing the effect of stimulus repetitions, every image plane was acquired 2-4 times. Since the same cells were imaged in 2-3 planes, the stimulus was presented to, and responses were measured from, each cell 4-12 times. In the experiments testing the effect of stimulus repetitions, the stimulus was repeated and the images were acquired six times in each image plane.

Online response detection

The sequence of images acquired in an experiment was stored in a 3D data cube in which the first two dimensions correspond to the rows and columns of one two-photon image, and the third dimension corresponded to the time the image was acquired. In the data cube, calcium transients were treated as 3D objects. To detect the 3D location of the calcium transients, the data cube was first filtered using the Wiener filter, the result was thresholded at $2 \times$ the standard deviation (s.d.), and shot noise was reduced by applying a binary opening operator followed by a closing operator. In the resulting binary 3D data cube, 3D-continuous objects were detected using a connected-feature detection algorithm. To remove small transients, the object set was further filtered by setting a threshold on the spatial projections of the objects ($> 3.6 \mu\text{m}$ or 3 pixels) and on the temporal projection (decay time $> 1 \text{ s}$). Next, all objects were projected onto the 2D spatial plane, resulting in a connected pixel set for

each object. Independent component analysis was then performed on the original time series of measured fluorescence at these pixel sets for each object. This step connected together those pixels where responses were correlated in time. We kept those independent components as response transients where the amplitude distribution was skewed towards high amplitudes. This was done by setting a threshold for the skew and kurtosis of the distribution. The 2D spatial pixel sets belonging to the independent component responses were defined as ‘responding cells’. The response of a responding cell was expressed as $\Delta F/F$, where F was defined as either the location of the peak on the histogram of recorded fluorescence values from the responding cell, or the mean of the fluorescence values acquired before the beginning of the stimulation: the smaller of the two quantities was used. The activity traces of responding objects were determined online during recording using Python. Finding all responding objects and displaying the responses took less than half the data collection time. Based on the two-photon images, the responding objects were manually classified as cell bodies or dendrites. Apart from LGN data, all analyses and data presented in the paper are based on responses from cell bodies.

Cortical response quantification

For each response belonging to a cell body, motion-response amplitudes were assigned for each motion direction. The motion-response amplitude value for each direction of motion was determined by sorting all the recorded data points during image motion in a particular direction, and taking the mean of the larger half. For each cell in a recording, a response threshold was defined as the average of the response values recorded before the start of visual stimulation $+ 4 \times \text{s.d.}$ The cell was classified as ‘responding’ if its response to the stimulus moving in any of the directions was above the response threshold for a contiguous block of at least 1 s for at least two repetitions of the stimulus.

The direction selectivity index (DSI) and orientation selectivity index (OSI) were defined as described for retinal cells.

The “peak response” of a cortical cell in a given stimulus direction was defined similarly to the “peak firing rate” of a ganglion cell recorded *ex vivo*, except that here the maxima of the $\Delta F/F$ response curves obtained during repeated stimulus presentations were averaged.

The “mean of the peak response” and the “normalized mean of the peak response” of a group of cortical cells were determined similarly to the “mean of the peak firing rate” and “normalized mean of the peak firing rate” for retinal ganglion cells. Normalized means of the peak responses were plotted on polar plots in Supplementary Fig. 7a,d.

The horizontal versus vertical direction selectivity index was defined as:

$$\text{HVI} = \frac{N_H - N_V}{N_H + N_V}$$

Where N_H and N_V denote the number of cells preferring horizontal or vertical directions respectively (Figs. 5f, 6f, Supplementary Figs. 8c,f, 9c,f,i,l,o). Alternatively, the horizontal versus vertical direction selectivity index was defined for the mean of the peak responses

using the same equations but N_H and N_V were used to denote the mean of the peak responses in horizontal or vertical directions respectively (Supplementary Fig. 7c,f).

The “complementary cumulative distribution of DSI values” of a group of cortical cells was determined as described for retinal ganglion cells *ex vivo* but here, instead of the peak firing rates, the peak responses were used. Complementary cumulative distributions of DSI values are shown in Figs. 5g, 6g, Supplementary Fig. 10.

The posterior component of the responses of cortical DS cells was computed by taking posterior $\pm 45^\circ$ direction preferring cortical DS cells and summing the projection of their response amplitudes on the posterior axis. This sum was normalized by the number of cells in each condition. The posterior component of the responses of cortical DS cells is shown in Fig. 7.

LGN response quantification

We used the same procedure as described for cortical cells to obtain responding objects. Based on the two-photon images, the responding objects were manually classified as axon terminals. F/F response curves and response amplitudes of axon terminals were defined as described for cortical cells.

The “peak response” of a ganglion cell axon terminal within the LGN in a given stimulus direction was defined similarly to the “peak firing rate” of a ganglion cell recorded *ex vivo*, except here the maxima of the F/F response curves obtained during repeated stimulus presentations were averaged.

The “complementary cumulative distribution of DSI values” of a group of retinal ganglion cell axon terminals in the LGN was determined as described for retinal ganglion cells *ex vivo* but here, instead of the peak firing rates, the peak responses were used. Complementary cumulative distributions of DSI values are shown in Fig. 4d.

The “complementary cumulative distribution of peak responses across all stimulus directions” of a group of retinal ganglion cell axon terminals in the LGN was determined as described for retinal ganglion cells *ex vivo* but here, instead of the peak firing rates, the peak responses were used. These distributions are plotted in Fig. 4e.

Statistics

We used the following notations. n.s.: $p \geq 0.05$; *: $0.05 > p \geq 0.01$, **: $0.01 > p \geq 0.001$, ***: $p < 0.001$. s.e.m: standard error of the mean, s.d.: standard deviation. In boxplots, bottom and top whiskers: minimum and maximum; bottom and top of the rectangle: first and third quartiles; central line: median. We used the following statistical tests: Kolmogorov-Smirnov test, Mann-Whitney U test (one-tailed), Hodges-Ajne test, Fisher's exact test, Kruskal-Wallis H test. No statistical methods were used to pre-determine sample sizes but our sample sizes are similar to those reported in previous publications^{16,43}. We did not use randomization; data collection and analysis were not performed blind to the conditions of the experiments. Data was not excluded from analysis.

Supplementary Material

Refer to Web version on PubMed Central for supplementary material.

Acknowledgements

We thank J. Letzkus, M. Hübener, A. Kreile, G. Keller, J. Randall, and A. Holtmaat for helping with two-photon imaging and surgery; N. Cesarovic for advice concerning anesthesia; F. Franke and U. Mueller for helping with spike sorting; C. Patino Alvarez for helping with virus production; P. Argast for technical assistance; S. Oakeley, A. Wertz and A. Attinger for commenting on the manuscript. We acknowledge the following grants: Marie Curie IEF and EMBO LTF to D.H.; Boehringer Ingelheim Fonds PhD fellowship for A.D.; Human Frontier Science Program Postdoctoral Fellowship and Ambizione Fellowship to S.T.; Swiss National Science Foundation, European Research Council, National Centres of Competence in Research Molecular Systems Engineering, Swiss National Science Foundation Sinergia, Swiss-Hungarian, DARPA, and European Union 3X3D Imaging grants to B.R. The ETH Zurich group, M.F. and A.H. acknowledge funding through the European Research Council Advanced Grant "NeuroCMOS", contract number AdG 267351, and the Swiss National Science Foundation Sinergia Project CRSII3_141801.

References

- Hubel DH, Wiesel TN. Receptive fields of single neurones in the cat's striate cortex. *J Physiol.* 1959; 148:574–591. [PubMed: 14403679]
- Hubel DH, Wiesel TN. Receptive fields, binocular interaction and functional architecture in the cat's visual cortex. *The Journal of physiology.* 1962; 160:106. [PubMed: 14449617]
- Priebe NJ, Ferster D. Direction selectivity of excitation and inhibition in simple cells of the cat primary visual cortex. *Neuron.* 2005; 45:133–145. [PubMed: 15629708]
- Stanley GB, et al. Visual Orientation and Directional Selectivity through Thalamic Synchrony. *J Neurosci.* 2012; 32:9073–9088. [PubMed: 22745507]
- Wei W, Feller MB. Organization and development of direction-selective circuits in the retina. *Trends Neurosci.* 2011; 34:638–645. [PubMed: 21872944]
- Vaney DI, Sivyer B, Taylor WR. Direction selectivity in the retina: symmetry and asymmetry in structure and function. *Nat Rev Neurosci.* 2012; 13:194–208. [PubMed: 22314444]
- Huberman AD, et al. Genetic Identification of an On-Off Direction-Selective Retinal Ganglion Cell Subtype Reveals a Layer-Specific Subcortical Map of Posterior Motion. *Neuron.* 2009; 62:327–334. [PubMed: 19447089]
- Kay JN, et al. Retinal ganglion cells with distinct directional preferences differ in molecular identity, structure, and central projections. *J Neurosci.* 2011; 31:7753–7762. [PubMed: 21613488]
- Rivlin-Etzion M, et al. Transgenic mice reveal unexpected diversity of on-off direction-selective retinal ganglion cell subtypes and brain structures involved in motion processing. *J Neurosci.* 2011; 31:8760–8769. [PubMed: 21677160]
- Fiscella M, et al. Recording from defined populations of retinal ganglion cells using a high-density CMOS-integrated microelectrode array with real-time switchable electrode selection. *Journal of Neuroscience Methods.* 2012; 211:103–113. [PubMed: 22939921]
- Weng S, Sun W, He S. Identification of ON-OFF direction-selective ganglion cells in the mouse retina. *J Physiol (Lond.).* 2005; 562:915–923. [PubMed: 15564281]
- Marshel JH, Kaye AP, Nauhaus I, Callaway EM. Anterior-posterior direction opponency in the superficial mouse lateral geniculate nucleus. *Neuron.* 2012; 76:713–720. [PubMed: 23177957]
- Piscopo DM, El-Danaf RN, Huberman AD, Niell CM. Diverse visual features encoded in mouse lateral geniculate nucleus. *J Neurosci.* 2013; 33:4642–4656. [PubMed: 23486939]
- Cruz-Martín A, et al. A dedicated circuit links direction-selective retinal ganglion cells to the primary visual cortex. *Nature.* 2014; 507:358–361. [PubMed: 24572358]
- Sun W, Tan Z, Mensh BD, Ji N. Thalamus provides layer 4 of primary visual cortex with orientation- and direction-tuned inputs. *Nat Neurosci.* 2016; 19:308–315. [PubMed: 26691829]
- Yonehara K, et al. Congenital Nystagmus Gene FRMD7 Is Necessary for Establishing a Neuronal Circuit Asymmetry for Direction Selectivity. *Neuron.* 2016; 89:177–193. [PubMed: 26711119]

17. Yoshida K, et al. A Key Role of Starburst Amacrine Cells in Originating Retinal Directional Selectivity and Optokinetic Eye Movement. *Neuron*. 2001; 30:771–780. [PubMed: 11430810]
18. Ivanova E, Hwang G-S, Pan Z-H. Characterization of transgenic mouse lines expressing Cre recombinase in the retina. *Neuroscience*. 2010; 165:233–243. [PubMed: 19837136]
19. Buch T, et al. A Cre-inducible diphtheria toxin receptor mediates cell lineage ablation after toxin administration. *Nat Methods*. 2005; 2:419–426. [PubMed: 15908920]
20. Trenholm S, Johnson K, Li X, Smith RG, Awatramani GB. Parallel mechanisms encode direction in the retina. *Neuron*. 2011; 71:683–694. [PubMed: 21867884]
21. Müller J, et al. High-resolution CMOS MEA platform to study neurons at subcellular, cellular, and network levels. *Lab Chip*. 2015; 15:2767–2780. [PubMed: 25973786]
22. Venkataramani S, Taylor WR. Orientation Selectivity in Rabbit Retinal Ganglion Cells Is Mediated by Presynaptic Inhibition. *J Neurosci*. 2010; 30:15664–15676. [PubMed: 21084622]
23. Nath A, Schwartz GW. Cardinal Orientation Selectivity Is Represented by Two Distinct Ganglion Cell Types in Mouse Retina. *J Neurosci*. 2016; 36:3208–3221. [PubMed: 26985031]
24. Güler AD, et al. Melanopsin cells are the principal conduits for rod–cone input to non-image-forming vision. *Nature*. 2008; 453:102–105. [PubMed: 18432195]
25. Chen T-W, et al. Ultrasensitive fluorescent proteins for imaging neuronal activity. *Nature*. 2013; 499:295–300. [PubMed: 23868258]
26. Deverman BE, et al. Cre-dependent selection yields AAV variants for widespread gene transfer to the adult brain. *Nat Biotech*. 2016; 34:204–209.
27. Hagihara KM, Murakami T, Yoshida T, Tagawa Y, Ohki K. Neuronal activity is not required for the initial formation and maturation of visual selectivity. *Nat Neurosci*. 2015; 18:1780–1788. [PubMed: 26523644]
28. Keck T, et al. Synaptic Scaling and Homeostatic Plasticity in the Mouse Visual Cortex In Vivo. *Neuron*. 2013; 80:327–334. [PubMed: 24139037]
29. Hengen KB, Torrado Pacheco A, McGregor JN, Van Hooser SD, Turrigiano GG. Neuronal Firing Rate Homeostasis Is Inhibited by Sleep and Promoted by Wake. *Cell*. 2016; 165:180–191. [PubMed: 26997481]
30. Hoggarth A, et al. Specific wiring of distinct amacrine cells in the directionally selective retinal circuit permits independent coding of direction and size. *Neuron*. 2015; 86:276–291. [PubMed: 25801705]
31. Farrow K, et al. Ambient illumination toggles a neuronal circuit switch in the retina and visual perception at cone threshold. *Neuron*. 2013; 78:325–338. [PubMed: 23541902]
32. Siebert S, et al. Genetic address book for retinal cell types. *Nat Neurosci*. 2009; 12:1197–1204. [PubMed: 19648912]
33. Fiscella M, et al. Recording from defined populations of retinal ganglion cells using a high-density CMOS-integrated microelectrode array with real-time switchable electrode selection. *Journal of Neuroscience Methods*. 2012; 211:103–113. [PubMed: 22939921]
34. Frey U, Egert U, Heer F, Hafizovic S, Hierlemann A. Microelectronic system for high-resolution mapping of extracellular electric fields applied to brain slices. *Biosens Bioelectron*. 2009; 24:2191–2198. [PubMed: 19157842]
35. Franke F, Quiñero R, Hierlemann A, Obermayer K. Bayes optimal template matching for spike sorting - combining fisher discriminant analysis with optimal filtering. *J Comput Neurosci*. 2015; 38:439–459. [PubMed: 25652689]
36. Mazurek M, Kager M, Van Hooser SD. Robust quantification of orientation selectivity and direction selectivity. *Front Neural Circuits*. 2014; 8
37. Grieger JC, Choi VW, Samulski RJ. Production and characterization of adeno-associated viral vectors. *Nat Protoc*. 2006; 1:1412–1428. [PubMed: 17406430]
38. Holtmaat A, et al. Long-term, high-resolution imaging in the mouse neocortex through a chronic cranial window. *Nat Protoc*. 2009; 4:1128–1144. [PubMed: 19617885]
39. Cahill H, Nathans J. The optokinetic reflex as a tool for quantitative analyses of nervous system function in mice: application to genetic and drug-induced variation. *PLoS ONE*. 2008; 3:e2055. [PubMed: 18446207]

40. Yonehara K, et al. Identification of retinal ganglion cells and their projections involved in central transmission of information about upward and downward image motion. *PLoS ONE*. 2009; 4:e4320. [PubMed: 19177171]
41. Remtulla S, Hallett PE. A schematic eye for the mouse, and comparisons with the rat. *Vision Res*. 1985; 25:21–31. [PubMed: 3984214]
42. Yardeni T, Eckhaus M, Morris HD, Huizing M, Hoogstraten-Miller S. Retro-orbital injections in mice. *Lab Anim (NY)*. 2011; 40:155–160. [PubMed: 21508954]
43. Ohki K, Chung S, Chng YH, Kara P, Reid RC. Functional imaging with cellular resolution reveals precise micro-architecture in visual cortex. *Nature*. 2005; 433:597–603. [PubMed: 15660108]

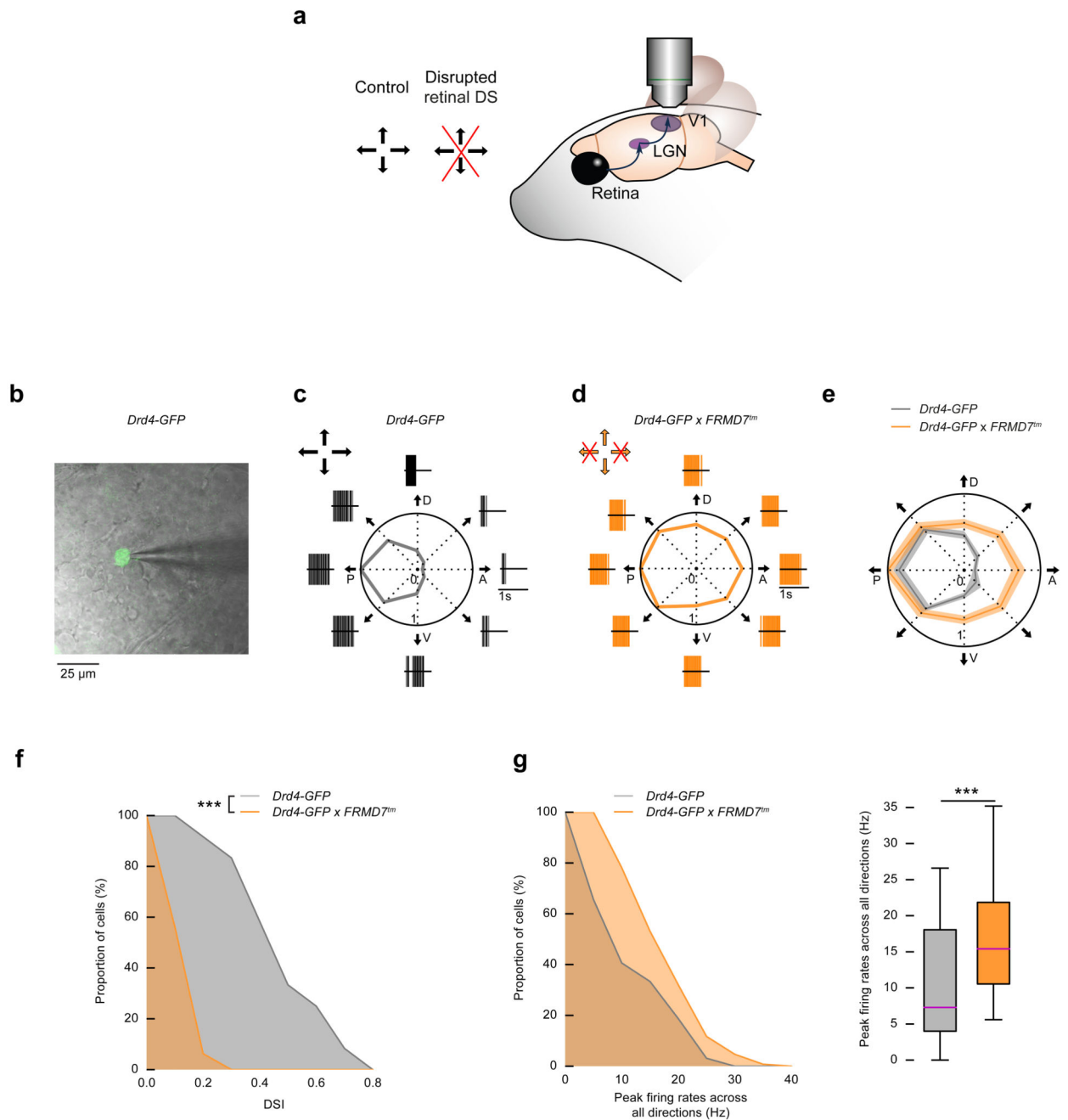


Figure 1. *FRMD7* mutation leads to spiking in all directions in posterior-direction-preferring retinal ON-OFF DS cells.

(a) Schematic of the experimental strategy throughout the paper. In the retina of control mice, ON-OFF DS cells prefer one of four cardinal directions (black arrows). The effect of disrupted retinal direction selectivity (red cross) is recorded in the retina, LGN, and V1. (b-g) Targeted patch clamp recordings in the retina. Control mice: *Drd4-GFP*, mutant mice: *Drd4-GFP* × *FRMD7^{mm}*. (b) A two-photon image of a GFP-labeled ganglion cell (green) in control retina is overlaid with the infrared image of the ganglion cell layer and a patch

pipette (grey). **(c-d)** Example responses from GFP-labeled ganglion cells in control **(c)** and mutant **(d)** retinas to a stimulus moving in eight directions (black arrows). P denotes posterior, D dorsal, A anterior, V ventral motion direction in the visual field. Polar plots show the normalized peak firing rates (Methods) in each stimulus direction. Spike raster plots around polar plots show single trial responses. Arrows at the top left corner of **c** and **d** indicate the preferred directions of direction selective retinal ganglion cells. Crossed arrows: missing direction selectivity in that direction. **(e)** Polar plot of the normalized mean of the peak firing rates (Methods) in control and mutant retinas. The width of the grey and orange bands corresponds to $2 \times \text{s.e.m.}$ **(f)** The proportion of GFP-labeled ganglion cells (indicated on the y-axis) with DSI larger than a specified value (indicated on the x-axis) in control and mutant retinas (complementary cumulative distribution of DSI values). **(g)** Left, complementary cumulative distribution of peak firing rates across all stimulus directions recorded from GFP-labeled ganglion cells in control and mutant retinas. Right, the boxplot representation of the distributions. Bottom and top whiskers: minimum and maximum; bottom and top of the rectangle: first and third quartiles; central line: median.

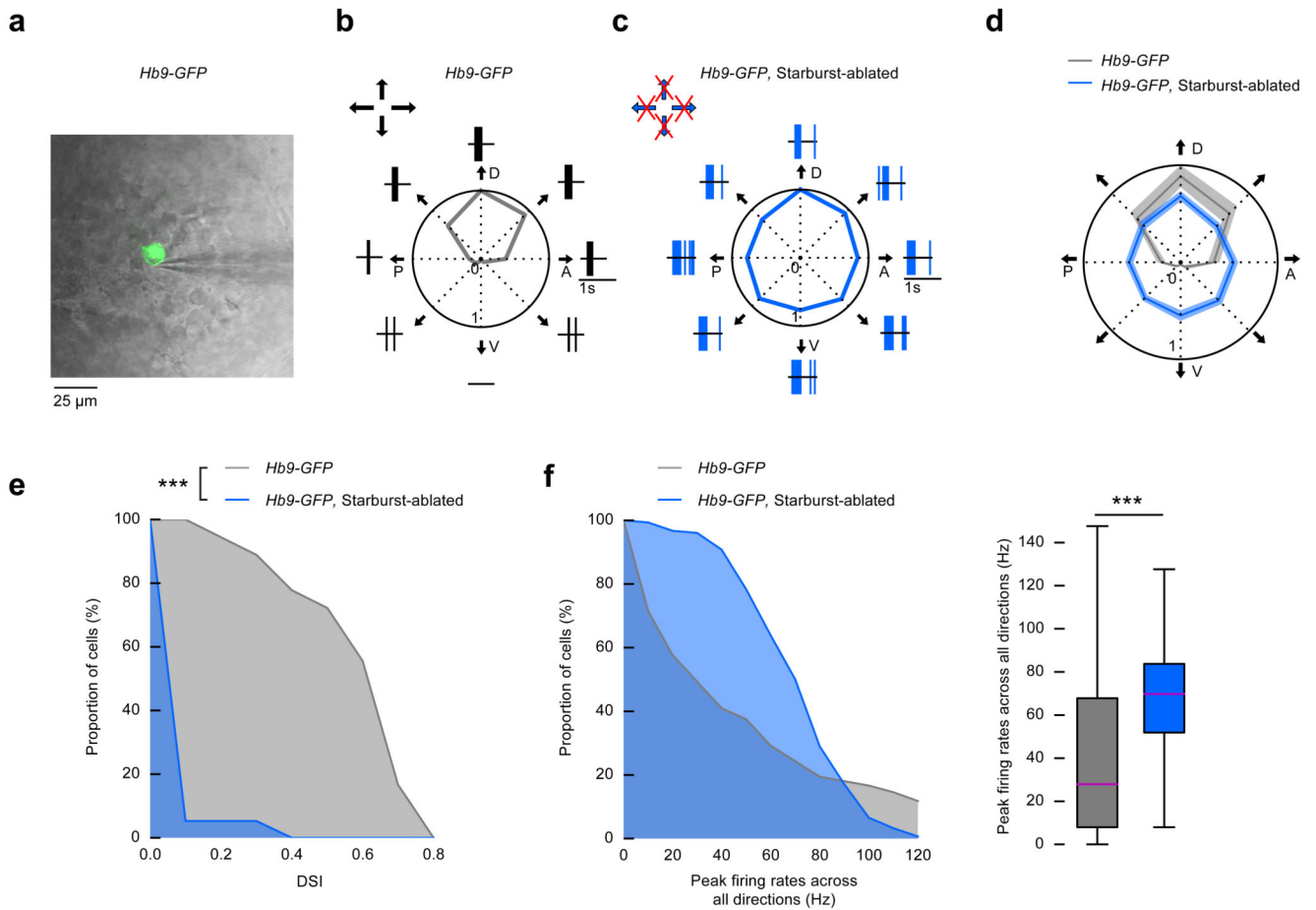


Figure 2. Starburst cell ablation leads to spiking in all directions in dorsal-direction-preferring retinal ON-OFF DS cells.

(a-f) Control mice: *Hb9-GFP* injected with DT, starburst-ablated mice: *Hb9-GFP* × *ChAT-Cre* × *LSL-DTR* injected with DT. (a) A two-photon image of a GFP-labeled ganglion cell (green) in control retina is overlaid with the infrared image of the ganglion cell layer and a patch pipette (grey). (b-c) Example responses from GFP-labeled ganglion cells in control (b) and starburst-ablated (c) retinas to a stimulus moving in eight directions (black arrows). P denotes posterior, D dorsal, A anterior, V ventral motion direction in the visual field. Polar plots show the normalized peak firing rates in each stimulus direction. Spike raster plots around polar plots show single trial responses. Arrows at the top left corner of b and c indicate the preferred directions of direction selective retinal ganglion cells. Crossed arrows: missing direction selectivity in that direction. (d) Polar plot of the normalized mean of the peak firing rates of all the recorded cells in control and starburst-ablated retinas. The width of the grey and blue bands corresponds to $2 \times$ s.e.m. (e) Complementary cumulative distributions of DSI values of recorded GFP-labeled ganglion cells in control and starburst-ablated retinas. (f) Left, complementary cumulative distributions of peak firing rates across all stimulus directions recorded from GFP-labeled ganglion cells in control and starburst-ablated retinas. Right, the boxplot representation of the distributions. Bottom and top

whiskers: minimum and maximum; bottom and top of the rectangle: first and third quartiles;
central line: median.

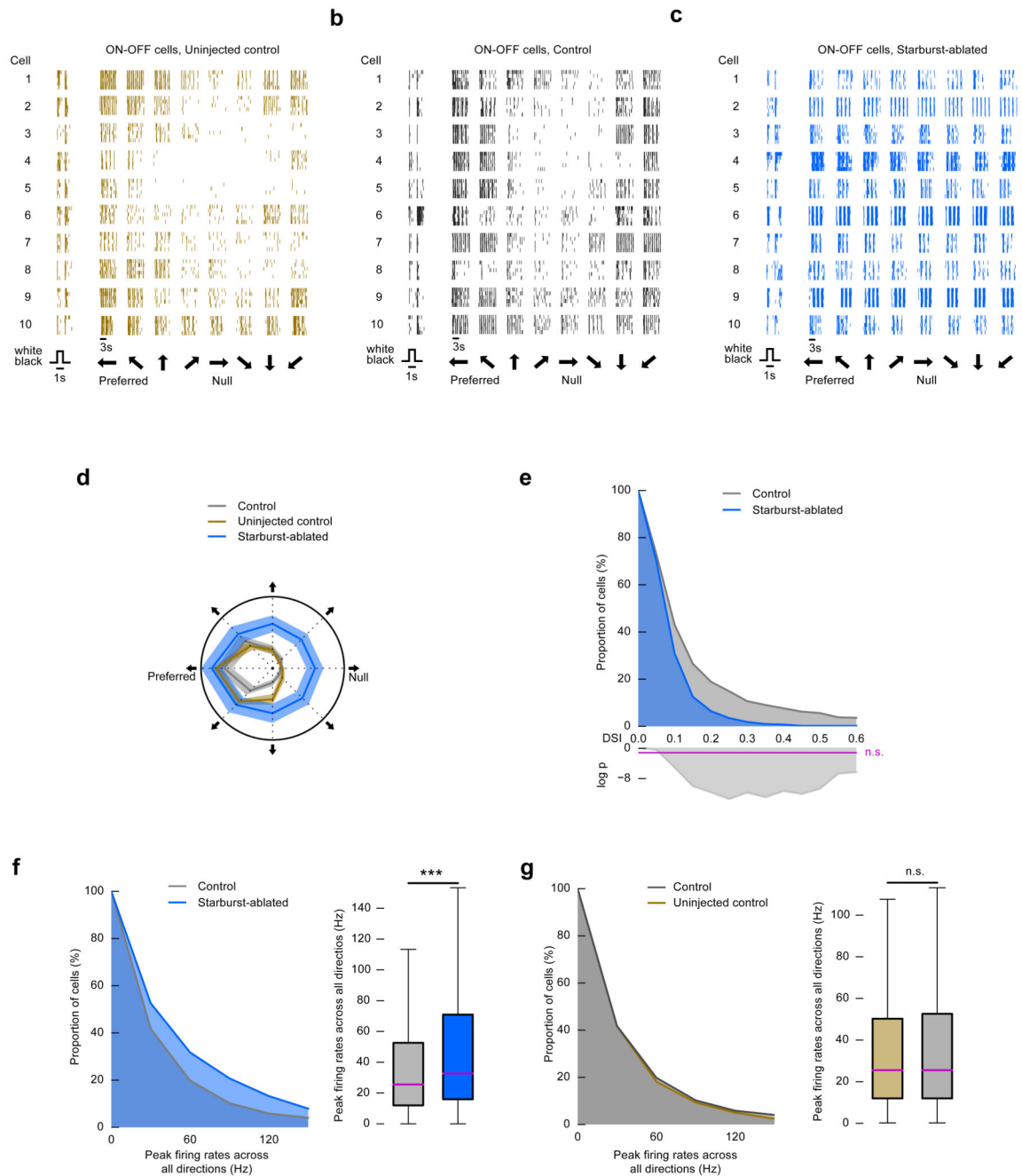


Figure 3. Direction selectivity is largely reduced in starburst-ablated retinas.

(a-g) Microelectrode array recordings of the retina. Uninjected control mice: wild type, control mice: wild type injected with DT, starburst-ablated mice: *ChAT-Cre* × *LSL-DTR* injected with DT. (a-c) Example responses from ten ON-OFF ganglion cells in uninjected control (a), control (b), and mutant (c) retinas to a flashed positive-contrast stimulus (timing is shown at the bottom) and a stimulus moving in eight directions (black thick arrows at the bottom). During motion stimulation, each block shows the response of a cell to motion in one of eight different directions. Each block has five rows representing five responses of the

same cell to repeated stimulus presentations. Vertical lines mark spike occurrences. **(d)** Polar plot of the normalized mean of the peak firing rates of the recorded cells **(a-c)** in uninjected control, control, and mutant retinas. The width of the grey, blue and brown bands corresponds to $2 \times \text{s.e.m.}$ **(e)** Top, the complementary cumulative distribution of DSI values of recorded ganglion cells in control and starburst-ablated mice. Bottom, the logarithm of p values comparing the pairs of conditions using Fisher's exact test. Values above the magenta line are non-significant. **(f)** Left, complementary cumulative distributions of peak firing rates across all stimulus directions in control and starburst-ablated retinas. Right, the boxplot representation of the distributions. Bottom and top whiskers: minimum and maximum; bottom and top of the rectangle: first and third quartiles; central line: median. **(g)** Left, complementary cumulative distributions of peak firing rates across all stimulus directions in uninjected control and control retinas. Right, the boxplot representation of the distributions.

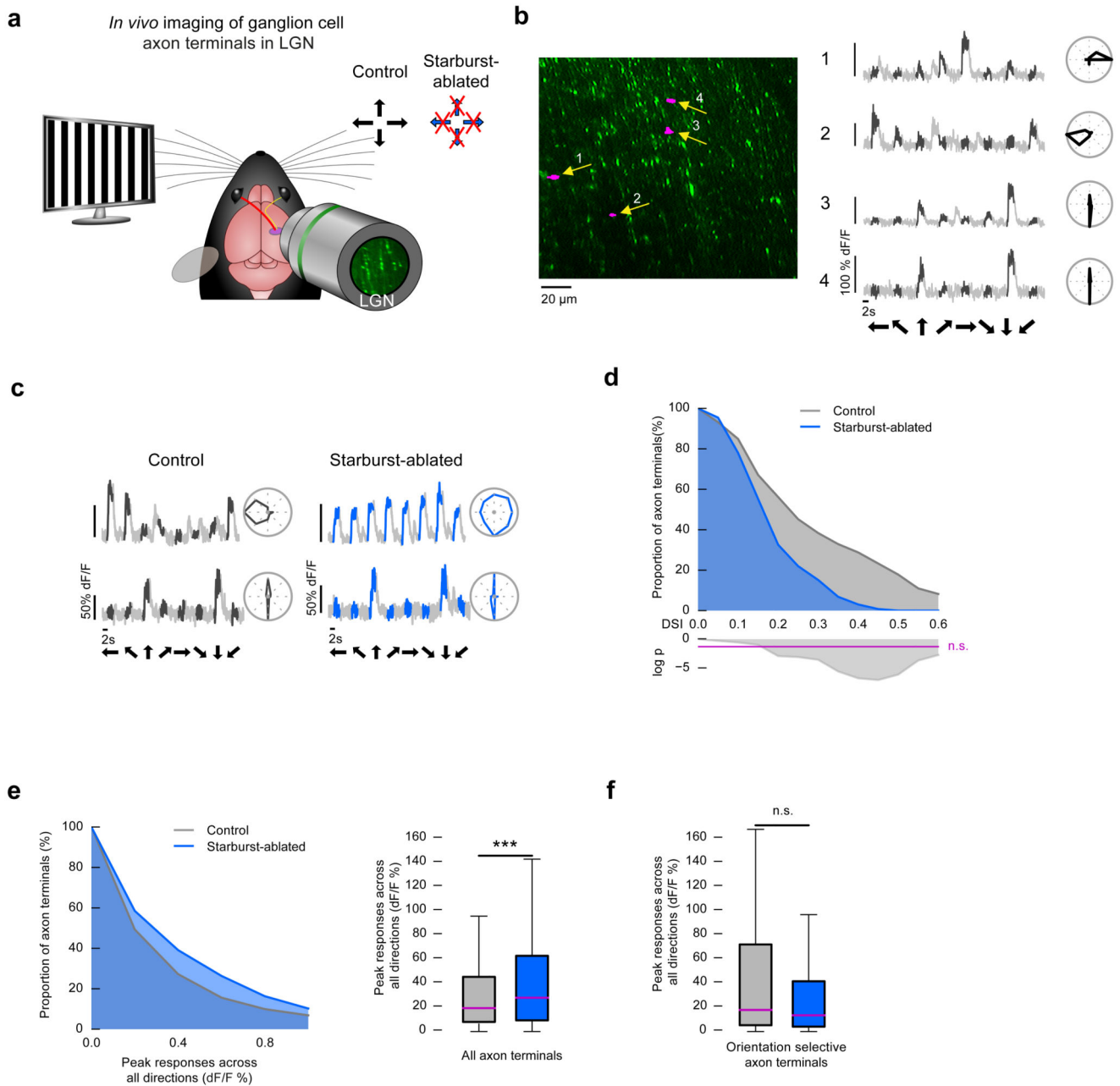


Figure 4. Starburst ablation reduces direction selectivity in retinal ON-OFF DS cells *in vivo*. (a-f) Two-photon imaging of ganglion cell axon terminals in the LGN. Control mice: wild type injected with DT, starburst-ablated mice: *ChAT-Cre* × *LSL-DTR* injected with DT. (a) Schematic of the experiment in the LGN. The stimulus was a grating drifting in eight directions. Responses of ganglion cell terminals in the LGN were measured in control and starburst-ablated mice. Arrows at the top right corner indicate the preferred directions of direction selective retinal ganglion cells. Crossed arrows: missing direction selectivity in that direction. (b) Left, two-photon image of GCaMP6s-labeled retinal ganglion cell axons in the LGN. Middle, examples of responses measured from control ganglion cell axon terminals

corresponding to the labeled regions on the image (magenta regions indicated by yellow arrows). Here and in subsequent panels, the black part of a grey trace shows the response during image motion in control mice and black arrows below the traces show the stimulus direction. Right: polar plots of response magnitudes normalized to the response in the preferred direction. **(c)** Responses to motion, and polar plots of responses of two retinal ganglion cell axon terminals recorded in the LGN of control (left) and starburst-ablated (right) mice. Blue part of the grey trace shows the response during image motion in starburst-ablated mice. Right of each curve: polar plots of response magnitudes normalized to the response in the preferred direction. **(d)** Top, complementary cumulative distributions of DSI values of recorded ganglion cell axon terminals in control and starburst-ablated mice. Bottom, the logarithm of p values comparing the pairs of conditions using Fisher's exact test. Values above the magenta line are non-significant. **(e)** Left, complementary cumulative distributions of peak responses across all stimulus directions in ganglion cell axon terminals of control and starburst-ablated mice. Right, boxplot representation of the distributions. Bottom and top whiskers: minimum and maximum; bottom and top of the rectangle: first and third quartiles; central line: median. **(f)** Boxplot representation of the distributions of peak responses across all stimulus directions within vertically oriented orientation-selective responses in control (grey) and starburst-ablated (blue) mice.

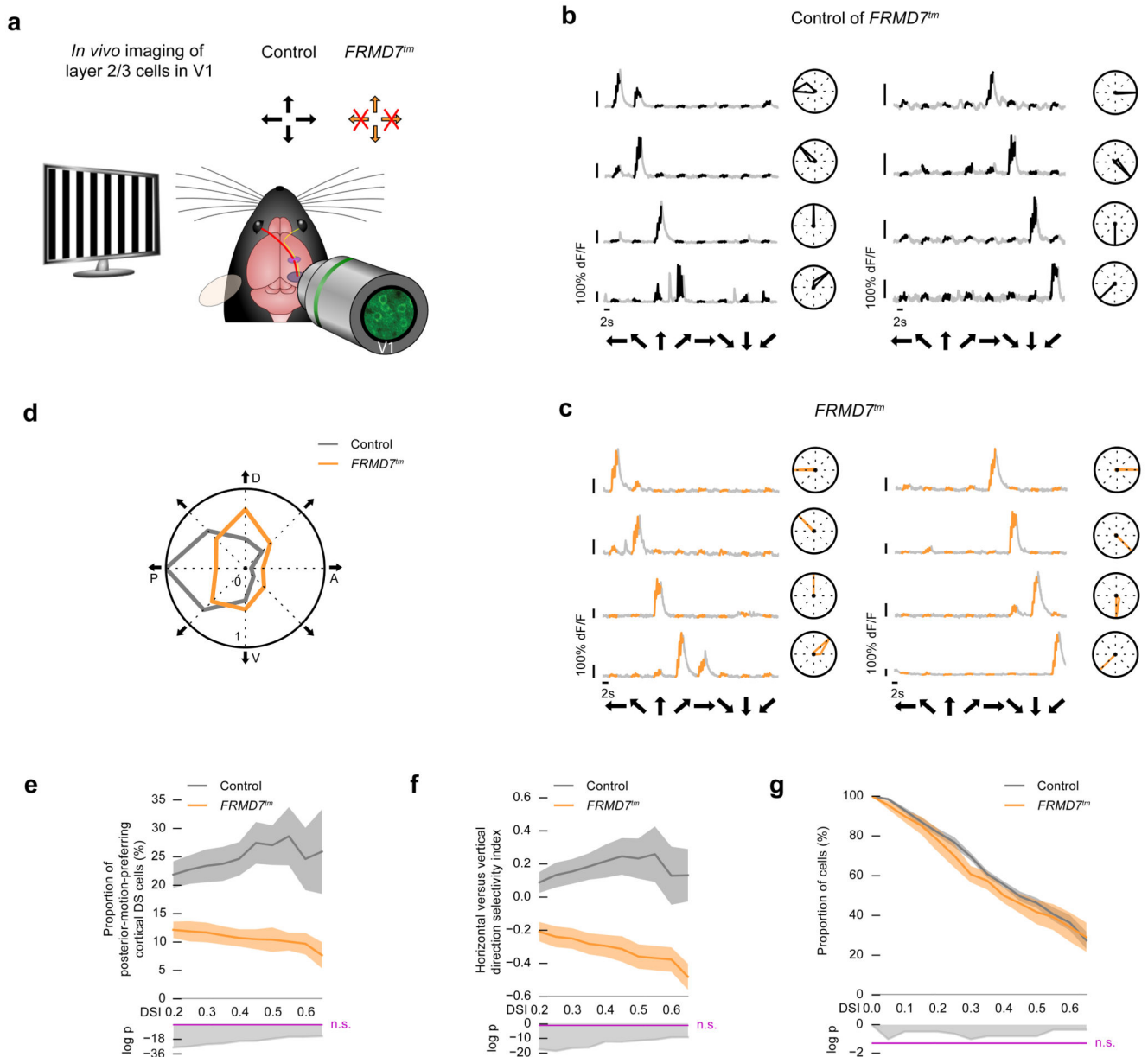


Figure 5. Disrupting retinal direction selectivity decreases the proportion of posterior-motion-prefering cortical DS cells in *FRMD7tm* mice.

(a) Schematic of the experiment in the cortex. Two-photon imaging cells in layer 2/3 of V1 in control mice and in *FRMD7tm* mice with disrupted retinal direction selectivity along the horizontal axis. The stimulus was a grating drifting in eight directions. Arrows at the top right corner indicate the preferred directions of direction selective retinal ganglion cells. Crossed arrows: missing direction selectivity in that direction. (b-g) Control mice: wild type, mutant mice: *FRMD7tm*. (b-c) Example responses from cortical DS cells recorded in control (b) and *FRMD7tm* (c) mice. Black (b) or orange (c) part of a grey trace shows the response during image motion. Black arrows below the traces show the stimulus direction. Right: polar plots of response magnitudes normalized to the response in the preferred direction. (d)

Polar plot showing the proportion of cortical DS cells preferring each of the stimulus directions in control and mutant mice. The proportions are normalized to the largest proportion across the two conditions. Cells with $DSI > 0.5$ are included in the plot. P denotes posterior, D dorsal, A anterior, V ventral motion direction in the visual field. **(e)** Top, proportion of posterior-motion-preferring cortical DS cells in control and mutant mice. Dark curves show mean values, shaded areas show \pm s.e.m around the means. Bottom, the logarithm of p values comparing the conditions using Fisher's exact test. Values above the magenta line are non-significant. The DSI values shown along the horizontal axis denote the DSI thresholds defining cells as direction selective. **(f)** Top, horizontal versus vertical direction selectivity index in control and mutant mice (Methods). Bottom, the logarithm of p values comparing the conditions using Fisher's exact test. Values above the magenta line are non-significant. The DSI values shown along the horizontal axis denote the DSI thresholds defining cells as direction selective. **(g)** Top, complementary cumulative distributions of DSI values of recorded cells in control and mutant mice. Bottom, the logarithm of p values comparing the conditions using Fisher's exact test. Values above the magenta line are non-significant.

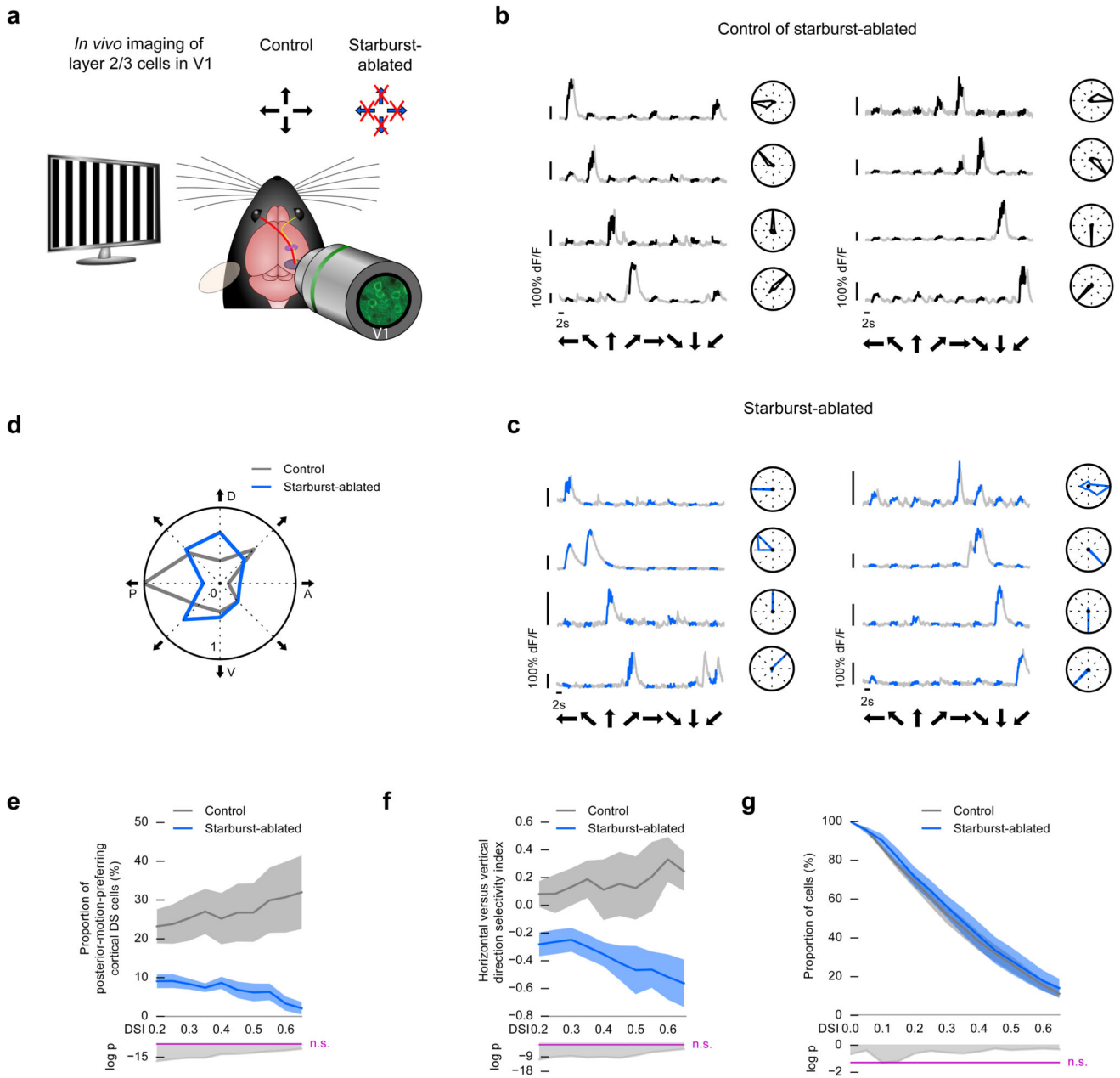


Figure 6. Disrupting retinal direction selectivity decreases the proportion of posterior-motion-prefering cortical DS cells in starburst-ablated mice.

(a) Schematic of the experiment in the cortex. Two-photon imaging cells in layer 2/3 of V1 in control mice and in starburst-ablated mice with disrupted retinal direction selectivity along both the horizontal and the vertical axes. The stimulus was a grating drifting in eight directions. Arrows at the top right corner indicate the preferred directions of direction selective retinal ganglion cells. Crossed arrows: missing direction selectivity in that direction. (b-g) Control mice: wild type injected with DT, starburst-ablated mice: *Chat-Cre* × *LSL-DTR* injected with DT. (b-c) Example responses from cortical DS cells recorded in control (b) and starburst-ablated (c) mice. Black (b) or blue (c) part of a grey trace shows the

response during image motion. Black arrows below the traces show the stimulus direction. Right: polar plots of response magnitudes normalized to the response in the preferred direction. **(d)** Polar plot showing the proportion of cortical DS cells preferring each of the stimulus directions in control and starburst-ablated mice. The proportions are normalized to the largest proportion across the two conditions. Cells with $DSI > 0.5$ are included in the plot. P denotes posterior, D dorsal, A anterior, V ventral motion direction in the visual field. **(e)** Top, proportion of posterior-motion-preferring cortical DS cells in control and starburst-ablated mice. Dark curves show mean values, shaded areas show \pm s.e.m around the means. Bottom, the logarithm of p values comparing the conditions using Fisher's exact test. Values above the magenta line are non-significant. The DSI values shown along the horizontal axis denote the DSI thresholds defining cells as direction selective. **(f)** Top, horizontal versus vertical direction selectivity index in control and starburst-ablated mice. Bottom, the logarithm of p values comparing the conditions using Fisher's exact test. Values above the magenta line are non-significant. The DSI values shown along the horizontal axis denote the DSI thresholds defining cells as direction selective. **(g)** Top, complementary cumulative distributions of DSI values of recorded cells in control and mutant mice. Bottom, the logarithm of p values comparing the conditions using Fisher's exact test. Values above the magenta line are non-significant.

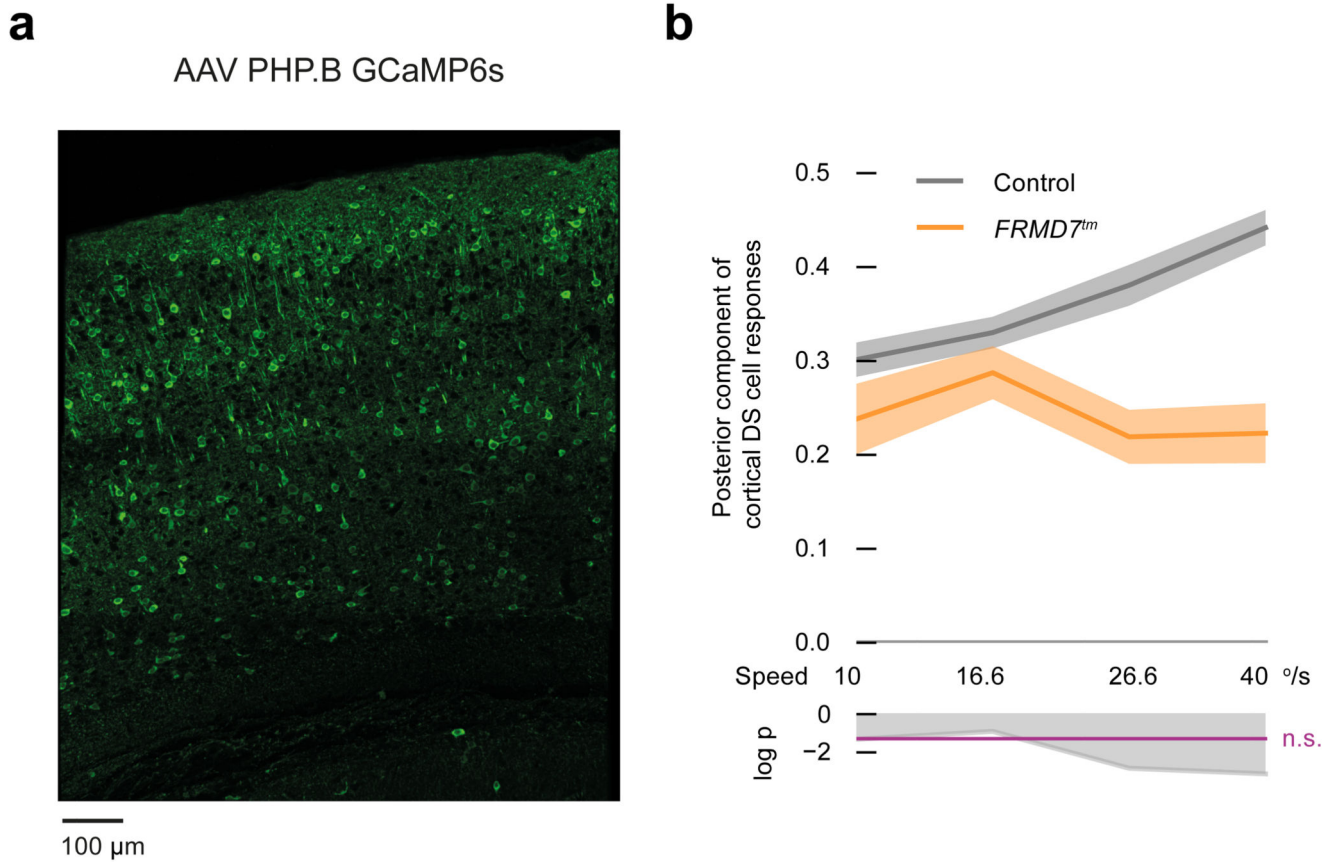


Figure 7. Posterior component of cortical DS cell responses is reduced at high stimulus speeds in *FRMD7tm* mice.

(a) Intravenous injection of AAV serotype PHP.B yields widespread expression of GCaMP6s in the cortex. Cortical slice stained with anti-GFP antibody (representing GCaMP6s expression) is shown. (b) Control mice: wild type, mutant mice: *FRMD7tm*. Top, posterior component of the responses of cortical DS cells (Methods). Dark curves show mean values, shaded areas show \pm s.e.m around the means. Bottom, the logarithm of p values comparing the conditions using the Mann-Whitney U test. Values above the magenta line are non-significant. The horizontal axis denotes the speed of the stimulus. Cells with DSI > 0.5 are included in the plot.